

Numerical study of ground-level distribution of firebrands generated by line fires

N. Sardoy^a, J.L. Consalvi^a, A. Kaiss^a, A.C. Fernandez-Pello^b, B. Porterie^{a,*}

^a IUSTI/UMR CNRS 6595, Université de Provence, 5 rue Enrico Fermi, 13453 Marseille cedex 13, France

^b Department of Mechanical Engineering, University of California at Berkeley, Berkeley, CA 94720-1740, USA

Received 24 September 2007; received in revised form 13 May 2008; accepted 16 May 2008

Available online 18 June 2008

Abstract

An analysis was conducted of the transport of burning brands by plumes above line fires in a crosswind. The characteristics of firebrands at landing and their ground distribution were particularly investigated. Calculations were performed with disk-shaped firebrands for fire intensities and wind speeds representative of moderate- to high-intensity surface wildfire scenarios, with partial to full crown involvement. For each fire scenario, 10,000 disk-shaped firebrands with different aspect ratios were detached from the top of the tree canopy. Initial firebrand location and properties were randomly generated. The results show that the normalized mass of firebrands that land in a flaming state correlates with the flight time normalized by $\rho_{w0}\tau_{f0}$ and in a charring state by $\rho_{w0}D_{f0}^{5/3}\tau_{f0}^{-1/6}$ (ρ_{w0} , τ_{f0} , and D_{f0} are the initial density, thickness, and diameter of the firebrand). This last parameter also influences whether the particle burns in flight or reaches the ground. Model results reveal a bimodal ground-level distribution of the released firebrands when both pyrolysis and char oxidation are present in the firebrand. Some of the brands, mostly in a flaming state, land at a short distance from the fire and other firebrands in charring state land at a long distance. It was found that the parameter $\rho_{w0}\tau_{f0}$ determines which firebrands will land in the short- and long-distance regions, and the char content v_c determines the separation between regions. The short-distance firebrands impact the ground frequently while still flaming, have a greater remaining mass, and consequently present the greater fire danger.

© 2008 The Combustion Institute. Published by Elsevier Inc. All rights reserved.

Keywords: Spotting; Wildland fire; Ground-level distribution; Plume

1. Introduction

In most wildland fires, fire spread is mainly controlled by convective and radiative heat transfer from

the burning fuel bed region to the unburned vegetation ahead of it. This form of fire propagation can be viewed as a short-range mechanism. However, another important mechanism of fire propagation that can occur under certain conditions takes place through mass transfer, and is known as “fire spotting.” This mechanism, which can significantly enhance the rate of fire spread, occurs when firebrands are lofted by the fire plume and transported

* Corresponding author. Fax: +33 491 106 969.

E-mail address: bernard.porterie@polytech.univ-mrs.fr (B. Porterie).

Nomenclature

b	plume width parameter	v_e	entrainment velocity
c_p	specific heat	V_f	firebrand volume
d	horizontal distance measured from the fire front	w_g	velocity along the plume trajectory
d_k	horizontal distance of the center of the x -axis interval $[d_k - \Delta d/2; d_k + \Delta d/2]$ from the fire front	x, y, z	Cartesian coordinates of the fixed system
d^*	separation distance between the short-distance and long-distance firebrand regions	x', y', z'	Cartesian coordinates attached to the brand
D_f	firebrand diameter	<i>Greek symbols</i>	
\mathbf{F}	force	α_i	incidence angle of disk-shaped firebrands
Fr	Froude number	Δd	size of intervals in the x -axis discretization
\mathbf{g}	gravity acceleration vector	Δh	heat of combustion
H	height at which the wind velocity is specified	θ	plume trajectory angle from the horizontal
I	fire intensity	λ	plume parameter (λ^2 : spreading ratio of mass and heat vs. momentum)
\mathbf{I}_f	moment of inertia	μ	viscosity, mean travel distance
\mathbf{K}	moment	ν_c	char content
K_{pz}	z -component of the pitching moment	ρ	density
K_{rz}	z -component of the moment due to resistance	σ	standard deviation of travel distance
L_c	characteristic length of the flow	χ_0	burning parameter, $\chi_0 = \rho_{w0} D_{f0}^{5/3} \tau_{f0}^{-1/6}$
M	mass of the firebrand	τ_{f0}	firebrand thickness
\dot{m}_e	mass flux of ambient air entrained into the plume	ω_f	firebrand spin
n_{int}	number of intervals of the “short-distance” firebrand distribution along the x -axis	<i>Subscripts</i>	
N	plume edge criterion ($R^2 = Nb^2$)	0	initial value
$N(d)$	number of firebrands landing at a distance d from the fire front	c	char
N_k	number of firebrands landing in the interval $[d_k - \Delta d/2; d_k + \Delta d/2]$	cr	critical
N_{sd}	total number of “short-distance” firebrands	D	drag
N_{tot}	total number of firebrands that land on the ground	f	firebrand
r	radial distance	film	gas property at film temperature
R	plume radius	final	value at landing
s	distance along plume trajectory	g	gas
T	temperature	G	gravitational
\mathbf{u}	velocity	L	lift
\mathbf{u}_{rel}	relative gas/particle velocity, $\mathbf{u}_{rel} = \mathbf{u}_g - \mathbf{u}_f$	p	pyrolysis
U_{wind}	wind speed at a height H	rel	relative velocity
		sd	short-distance firebrand
		w	wood
		∞	ambient
		<i>Superscripts</i>	
		*	plume excess value on the centerline
		–	plume average value

downwind to ignite secondary fires beyond the zone of direct heat transfer ignition by the main fire. Among the many factors that affect spotting are the weather, topography, and fuel properties, which include the energetic content of firebrands at landing

and the ignition propensity of the receptive fuel bed. Dense short-range spotting may occur continuously, while isolated spots may occasionally be ignited at longer distances, typically more than a hundred meters.

In order to understand how fire behavior is affected by spotting, it is important to know the ground-level distribution of firebrands and their potential to ignite receptive fuel beds. This requires predicting the trajectories of burning brands transported by the plume and the prevailing wind, as well as their state at landing (i.e., state of combustion, remaining mass, and temperature), together with the characteristics of the vegetation in the landing area. The trajectories and burning rates of firebrands lofted by fires have been studied by several researchers over the years. Tarifa et al. [1], Lee and Hellman [2], and Albini [3] considered spherical brands and provided methods for simulating their transport and burning rate. Woycheese and Pagni [4] followed disk-shaped firebrands released into a Baum–McCaffrey buoyant plume, neglecting wind effects on the plume. Anthenien et al. [5] used a buoyancy-dominated plume model assuming that the horizontal velocity of the plume was equal to the cross-wind velocity. By comparing trajectories for spherical, cylindrical, and disk geometries, they found that disks propagate the farthest and have the greatest remaining mass fraction at landing. Himoto and Tanaka [6], Sardoy et al. [7], and Koo et al. [8] studied the transport of disk-shaped firebrands using a CFD (computational fluid dynamics) model to predict the plume characteristics. With the exception of the work of Albini [3], all these studies considered axisymmetric fire plumes.

An aspect of the problem that still needs further attention is information about the distribution and characteristics of the firebrands at landing. This information is important for determining whether the firebrand has the potential capacity to ignite the receptive vegetation and consequently spot the fire. The present study focuses on this aspect of the problem. To determine firebrand trajectories, a line fire plume is considered rather than an axisymmetric plume, as it is more representative of a wildland fire. The dynamic and thermal properties of the fire plume are determined using an extended form of the model proposed by Mercer and Weber [9], which provides a Gaussian distribution of plume properties. Disk-shaped firebrands are considered, as they represent the highest potential risk for spotting [4,5]. The disk shape is an approximation of firebrands generated from burning bark. Firebrands with different diameters, densities, and thicknesses are assumed to be lofted by the plume in a random distribution, and their flight path is calculated using the relevant transport equations [7] but also considering that the disks undergo lift and rotation. A thermal degradation and combustion model of firebrands is applied to determine their characteristics at landing.

2. Models

A summarized description of the different models used to solve the problem of firebrand distribution and characteristics at landing is given below to complete the presentation, and references to a more detailed description of the models are given.

2.1. Plume model

An integral model was developed to describe the behavior of buoyant line plumes released into stratified crossflows. This model is an extension of that of Mercer and Weber [9], in which the top-hat self-similar profile is replaced by a more realistic Gaussian profile.

For the ambient conditions, a power-law wind profile was considered in order to describe the variation of wind velocity with height [9],

$$U_{\infty}(y) = U_{\text{wind}} \left(\frac{y}{H} \right)^{1/7}, \quad (1)$$

where U_{wind} is the wind speed measured at a height H , and y is measured from the ground level.

A stable thermal atmosphere was also assumed, leading to a decrease in the ambient temperature with height according to

$$T_{\infty}(y) = T_{\infty}(0) + \frac{dT_{\infty}}{dy} y, \quad (2)$$

where dT_{∞}/dy is the temperature gradient, known as the dry adiabatic lapse rate and usually taken as -9.98 K km^{-1} [10].

The governing equations of the plume were obtained by balancing fluxes of mass, momentum, and thermal energy for the control volume illustrated in Fig. 1.

To develop the corresponding equations for a Gaussian model, Davidson [11] assumed that plume properties vary in the cross-flow direction according to

$$w_g = U_{\infty} \cos \theta + w^* \exp\left(-\frac{r^2}{b^2}\right), \quad (3)$$

$$\rho_g = \rho_{\infty} + \rho^* \exp\left(-\frac{r^2}{\lambda^2 b^2}\right), \quad (4)$$

$$T_g = T_{\infty} + T^* \exp\left(-\frac{r^2}{\lambda^2 b^2}\right), \quad (5)$$

where the λ^2 parameter takes into account the different turbulent diffusivities of mass and heat versus momentum. The plume width parameter b is related

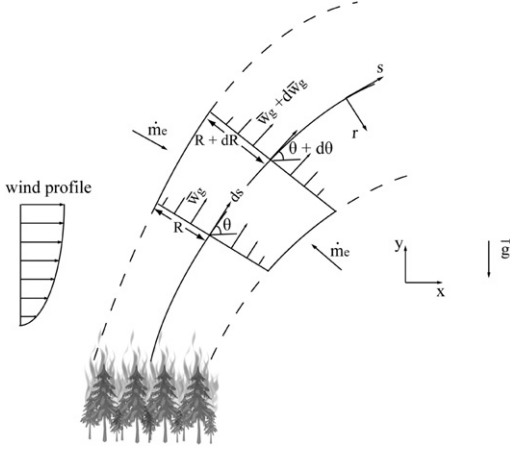


Fig. 1. Integral plume model: control volume used for the derivation of the conservation equations.

to the plume radius R by the assumption $R^2 = Nb^2$, with $N = 2$, as is usually chosen (e.g., [9,11]).

Average values of the plume in the cross-flow direction were obtained from the corresponding Gaussian variables through an area average. The average velocity relationship, for example, is given by

$$\bar{w}_g = \frac{1}{R} \int_0^R w_g dr, \quad (6)$$

which yields, after substitution of Eq. (3) and integration,

$$w^* = (\bar{w}_g - U_\infty \cos \theta) \frac{2\sqrt{N}}{\sqrt{\pi} \operatorname{erf}(\sqrt{N})}. \quad (7)$$

In the same way,

$$\rho^* = (\bar{\rho}_g - \rho_\infty) \frac{2\sqrt{N}}{\lambda \sqrt{\pi} \operatorname{erf}(\sqrt{N}/\lambda)} \quad (8)$$

$$T^* = (\bar{T}_g - T_\infty) \frac{2\sqrt{N}}{\lambda \sqrt{\pi} \operatorname{erf}(\sqrt{N}/\lambda)}. \quad (9)$$

The mass flux of ambient air entrained into the plume (Fig. 1) is given by

$$\dot{m}_e = 2\rho_\infty v_e. \quad (10)$$

Using the low-Mach-number approximation, the conservation equations of mass, s -momentum, r -momentum, and thermal energy for a control volume in the buoyant plume are then given by

$$\frac{d}{ds} \left(2 \int_0^R \rho_g w_g dr \right) = \dot{m}_e, \quad (11)$$

$$\begin{aligned} & \frac{d}{ds} \left(2 \int_0^R \rho_g w_g^2 dr \right) \\ &= \dot{m}_e U_\infty \cos \theta - 2 \int_0^R (\rho_g - \rho_\infty) g \sin \theta dr, \end{aligned} \quad (12)$$

$$\frac{d\theta}{ds} = - \frac{\dot{m}_e U_\infty \sin \theta + 2 \int_0^R (\rho_g - \rho_\infty) g \cos \theta dr}{2 \int_0^R \rho_g w_g^2 dr}, \quad (13)$$

$$\frac{d}{ds} \left(2 \int_0^R \rho_g w_g c_{pg} T_g dr \right) = \dot{m}_e c_{pg} T_\infty. \quad (14)$$

Substitution of Eqs. (3)–(5) and (10) and integration over r yields

$$\begin{aligned} & \frac{d}{ds} \{ \bar{\rho}_g \bar{w}_g b + (A_0 - 1)(\bar{w}_g - U_\infty \cos \theta)(\bar{\rho}_g - \rho_\infty) \} \\ &= \rho_\infty v_e, \end{aligned} \quad (15)$$

$$\begin{aligned} & \frac{d}{ds} \{ \bar{\rho}_g b \bar{w}_g^2 + (A_1 - 1) \rho_\infty b (\bar{w}_g - U_\infty \cos \theta)^2 \\ &+ (\bar{\rho}_g - \rho_\infty) b [(A_2 - A_0)(\bar{w}_g - U_\infty \cos \theta)^2 \\ &+ (A_0 - 1)(\bar{w}_g^2 - U_\infty^2 \cos^2 \theta)] \} = \rho_\infty v_e U_\infty \cos \theta \\ &- b g \sin \theta (\bar{\rho}_g - \rho_\infty), \end{aligned} \quad (16)$$

$$\frac{d\theta}{ds} = - \frac{\rho_\infty v_e U_\infty \sin \theta + (\bar{\rho}_g - \rho_\infty) b g \cos \theta}{\{ \}}, \quad (17)$$

$$\begin{aligned} & \frac{d}{ds} \{ \bar{\rho}_g b \bar{w}_g \Delta T + (A_0 - 1) \rho_\infty b \Delta T (\bar{w}_g - U_\infty \cos \theta) \\ &+ (A_3 - 1)(\bar{\rho}_g - \rho_\infty) b \Delta T U_\infty \cos \theta \\ &+ (\bar{\rho}_g - \rho_\infty) b (\bar{w}_g - U_\infty \cos \theta) \\ &\times [(A_4 - 1) \bar{T}_g - (A_4 - A_0) T_\infty] \} \\ &= T_\infty \frac{d}{ds} [(A_0 - 1) b (\bar{w}_g - U_\infty \cos \theta) \\ &\times (\bar{\rho}_g - \rho_\infty)] - \bar{\rho}_g b \bar{w}_g \frac{dT_\infty}{dy} \sin \theta \end{aligned} \quad (18)$$

with

$$A_0 = \frac{2\sqrt{N}}{\sqrt{\pi} \sqrt{\lambda^2 + 1}} \frac{\operatorname{erf}(\sqrt{N} \sqrt{1 + \lambda^2}/\lambda)}{\operatorname{erf}(\sqrt{N}) \operatorname{erf}(\sqrt{N}/\lambda)},$$

$$A_1 = \frac{\sqrt{2N}}{\sqrt{\pi}} \frac{\operatorname{erf}(\sqrt{2N})}{\operatorname{erf}^2(\sqrt{N})},$$

$$A_2 = \frac{4N}{\pi \sqrt{2\lambda^2 + 1}} \frac{\operatorname{erf}(\sqrt{N} \sqrt{2\lambda^2 + 1}/\lambda)}{\operatorname{erf}^2(\sqrt{N}) \operatorname{erf}(\sqrt{N}/\lambda)},$$

$A_3 = A_1/\lambda$, $A_4 = A_2/\lambda$, and $\Delta T = \bar{T}_g - T_\infty$. On the right-hand side of Eq. (17), the denominator is identical to the bracketed term on the left-hand side of Eq. (16).

In agreement with Davidson [11], the two-term entrainment hypothesis was retained and the air entrainment velocity is given by

$$v_e = N\alpha(\bar{w}_g - U_\infty \cos \theta) + \beta U_\infty \sin \theta, \quad (19)$$

where the constants have the values $\alpha = 0.057$ and $\beta = 0.5$.

In addition to these conservation laws, the plume model includes the kinematic relationships $dx = ds \cos \theta$, $dy = ds \sin \theta$ and an ideal gas law that is based on the approximation that the pressure inside the plume is equal to the ambient pressure.

Under the latter assumption and using Eqs. (4), (5), (8), and (9), the average density across the plume can be related to the average temperature by the relationship

$$\bar{\rho}_g = \rho_\infty \frac{T_\infty - A_5(T_\infty - \bar{T}_g)}{\bar{T}_g - A_5(T_\infty - \bar{T}_g)} \quad (20)$$

with

$$A_5 = \frac{2\sqrt{N}}{\lambda\sqrt{\pi} \operatorname{erf}(\sqrt{N}/\lambda)} - 1.$$

Finally, the x - and y -components of the gas velocity components are deduced from $u_{gx} = w_g \cos \theta$, $u_{gy} = w_g \sin \theta$.

2.2. Firebrand motion

The gas properties in the z -direction are invariant due to the line fire assumption, and thus the major axis direction of the firebrand, \mathbf{y}' , is assumed to be in the plane (xy) (see Fig. 1 in [7]). The motion of disk-shaped particles, including translation and rotation, is calculated by solving the conservation equations of kinematic and angular momentum,

$$\rho_f V_f \frac{d\mathbf{u}_f}{dt} = \mathbf{F}_D + \mathbf{F}_L + \mathbf{F}_G, \quad (21)$$

$$\mathbf{I}_f \frac{d\boldsymbol{\omega}_f}{dt} = \mathbf{K}, \quad (22)$$

where \mathbf{F}_D , \mathbf{F}_L , and \mathbf{F}_G are the drag, lift, and gravitational forces. Firebrand density, ρ_f , is directly related to virgin wood and char densities deduced from the thermal degradation and combustion model.

The moment of inertia with respect to the z -axis, I_{fz} , is given by

$$I_{fz} = \frac{\rho_f V_f}{8} \left(\frac{D_f^2}{2} + 2 \frac{\tau_{f0}^2}{3} \right). \quad (23)$$

In a gas/solid flow, the virtual mass effect and Basset history terms can be neglected because of the low gas-particle density ratio. For the same reason, the pressure gradient force is negligible compared with the drag and lift forces.

Drag, lift, and gravitational forces are expressed as

$$\mathbf{F}_D = \frac{1}{2} C_D \rho_{\text{film}} S_{\text{eff}1} \|\mathbf{u}_{\text{rel}}\| \mathbf{u}_{\text{rel}}, \quad (24)$$

$$\mathbf{F}_L = \frac{1}{2} C_L \rho_{\text{film}} S_{\text{eff}2} \frac{\mathbf{y}' \cdot \mathbf{u}_{\text{rel}}}{\|\mathbf{u}_{\text{rel}}\|} [\mathbf{y}' \times \mathbf{u}_{\text{rel}}] \times \mathbf{u}_{\text{rel}}, \quad (25)$$

$$\mathbf{F}_G = V_f (\rho_f - \rho_{\text{film}}) \mathbf{g}. \quad (26)$$

The subscript film indicates that the associated gas property is taken at the film temperature, which is the average between gas and particle surface temperatures. $S_{\text{eff}1}$ and $S_{\text{eff}2}$ are the particle areas normal to the directions of drag and lift forces, respectively. They depend on the incidence angle, α_i , between \mathbf{y}' and \mathbf{u}_{rel} [12],

$$S_{\text{eff}1} = \frac{\pi D_f^2}{4} \left[\sin^2 \alpha_i + \left(\frac{8\tau_{f0}}{\pi D_f} \right)^2 \cos^2 \alpha_i \right]^{1/2}, \quad (27)$$

$$S_{\text{eff}2} = \frac{\pi D_f^2}{4} \left[\cos^2 \alpha_i + \left(\frac{8\tau_{f0}}{\pi D_f} \right)^2 \sin^2 \alpha_i \right]^{1/2}. \quad (28)$$

Drag and lift coefficients are given as a function of both normal, C_N , and tangential, C_T , force coefficients [13],

$$C_D = C_N \sin \alpha_i - C_T \cos \alpha_i, \quad (29)$$

$$C_L = -C_N \cos \alpha_i - C_T \sin \alpha_i, \quad (30)$$

where

$$C_N = \frac{C_{D90} \sin \alpha_i}{0.56 + 0.44 \sin \alpha_i} \quad \text{and}$$

$$C_T = -0.00375 \cos \alpha_i.$$

C_{D90} is the two-dimensional drag force coefficient for an attack angle of 90° . It is given by

$$C_{D90} = 1.98 - 0.81 [1 - \exp(-20 D_f / \tau_f)].$$

The z -component of the resulting moment acting on the brand, K_z , is obtained by the sum of two torques. The first, called pitching moment K_{pz} , is due to the noncoincidence of the center of hydrodynamic forces and the center of mass [12],

$$K_{pz} = x_{cp} \mathbf{y}' \times (\mathbf{F}_D + \mathbf{F}_L) \cdot \mathbf{z}, \quad (31)$$

where the distance between the centers is given by

$$x_{cp} = 0.25 \frac{D_f}{2} [1 - \exp(1 - D_f / \tau_{f0})] [1 - \sin^3 \alpha_i].$$

The second, K_{rz} , is due to the resistance acting on a relatively rotating body, which contributes to the attenuation of relative rotation [12],

$$K_{rz} = \int_0^{D_f/2} C_D \rho_{\text{film}} \pi r^2 [(\omega_{gz} - \omega_{fz}) r]^2 dr, \quad (32)$$

where ω_{gz} represents the z -component of the local gas vorticity.

2.3. Firebrand burning

Details of the model and validation can be found in [7]. The main assumptions upon which the model is based are repeated below for the sake of completeness.

The firebrands are assumed to have been ignited and to be burning at the originating source. Pyrolysis is considered as a subsurface volumetric process whereas heterogeneous combustion (char oxidation) is considered as occurring at the outer surface of the particle. Consequently, the particle loses mass via in-depth pyrolysis and heterogeneous combustion, but it loses volume only from heterogeneous combustion. The pyrolysis front moves through the particle along its thickness. As regards the char oxidation, the particle loses volume only by diameter regression. During pyrolysis, the particle surface temperature remains constant and equal to 993 K [14]. Char oxidation can occur concomitantly with pyrolysis when oxygen reaches the char particle surface during the devolatilization stage.

If firebrands land before pyrolysis is complete, they will land at an elevated temperature; otherwise, they will land in a charring state with a temperature that depends on the energy balance between char oxidation and heat losses to the environment at the particle surface.

3. Results and discussions

3.1. Plume calculations

The solutions of 20 plumes that correspond to fire intensities of 10, 20, 30, and 40 MW m⁻¹, and wind speeds of 6.70, 8.94, 11.17, 13.41, 15.64, and 17.88 m s⁻¹ were computed. They are representative of moderate- to high-intensity surface fire scenarios, with partial to full crown involvement. The wind velocities were assumed to be those at the top of the tree canopy, $H = 10$ m, which was also considered as being the plume base. The ambient temperature was taken as equal to 300 K.

The solution of the plume requires the initial conditions for the plume inclination with the horizontal, θ , and the Gaussian temperature, velocity, and density distributions within the plume. For all cases, the average Gaussian temperature was taken as $\bar{T}_{g0} = 900$ K and the inclination angle as $\theta_0 = \pi/2$ [9]. As a first-order approximation, the mean specific heat of the gas was taken as that of air at \bar{T}_{g0} , which gives $c_{pg} = 1121$ kJ kg⁻¹ K⁻¹.

The initial width parameter and Gaussian velocity are related by the definition of fire intensity,

$$I = 2b_0\bar{w}_{g0}[c_{pg}\bar{\rho}_{g0}(\bar{T}_{g0} - T_{\infty})]. \quad (33)$$

This leads to

$$2b_0\bar{w}_{g0} = I/0.425 \quad (34)$$

with I in MW m⁻¹.

Preliminary calculations of gas velocity at the top of the canopy were first carried out for all the fire conditions under consideration using a physics-based three-dimensional wildland fire model [7]. It was found that the gas velocity on the centerline fell within the range 10.5–13 m s⁻¹. We therefore assumed that plume gases escape vertically from the canopy with a velocity on the centerline of 12 m s⁻¹, irrespective of fire conditions. This value and Eqs. (3) and (7) with $r = 0$ and $\theta_0 = \pi/2$ lead to an initial Gaussian velocity $\bar{w}_{g0} = 7$ m s⁻¹. For the 10, 20, 30, and 40 MW m⁻¹ fires considered, the initial width parameters deduced from Eq. (34) are therefore 1.68, 3.36, 5.04, and 6.72 m, respectively.

Calculations were then performed to compute thermal plume properties on a nonuniform mesh covering a large domain of 10×1.7 km². To simulate firebrand trajectories, 10,000 disk-shaped firebrands, with an initial aspect ratio τ_{f0}/D_{f0} ranging from 1 to 7.5%, were detached from randomly generated locations at the plume base. They were released into the precomputed plume with a random initial velocity between zero velocity and gas velocity. Initial firebrand location and properties were also randomly generated, in the range $-b$ to b along the plume width for its location, and 50 to 300 kg m⁻³ for its density, 1 to 3 mm for its thickness, 4 to 10 cm for its diameter, and 0° to 180° for the incidence angle. Firebrand properties are summarized in [7].

With a time step of 10^{-4} s, the solution was found to be time-step independent. The calculation of the 10,000 trajectories takes about 4 h of CPU time on a 32-processor SUN cluster (AMD X86, distributed memory).

3.2. Preliminary analysis

A dimensional analysis of the particle's kinetic momentum (Eq. (21)) shows that the group $\rho_{w0}\tau_{f0}$, being the ratio between the mass and surface of the firebrand, relates aerodynamic and gravitational forces, and thus controls the landing distance.

Existing results [7] showed that pyrolysis occurs in the thermally thin heat transfer regime, which indicates that pyrolysis time is proportional to the surface-to-mass ratio of the particle, and thus to the product $\rho_{w0}\tau_{f0}$ for a disk. As indicated previously, the model assumes that pyrolysis and char oxidation processes are concomitant. However, we showed [7] that, during pyrolysis, a small amount of oxygen diffuses toward

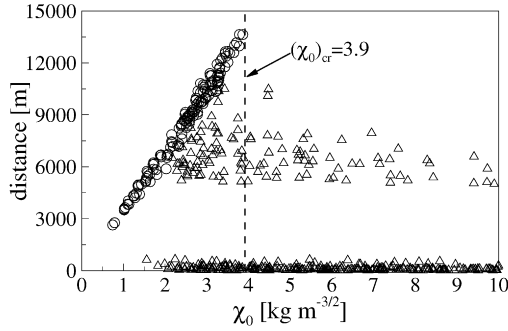


Fig. 2. The critical value of the burning parameter is determined graphically from the evolution of the distance traveled vs. χ_0 . Conditions are a fire intensity of 30 MW m^{-1} , a wind speed of 11.17 m s^{-1} , and $v_c = 0.39$. Circles correspond to firebrands that burn totally in the air, and triangles to firebrands that land on the ground.

the solid surface, which limits char oxidation in such a manner that the two processes can be considered as successive. It can thus be deduced that the parameter $\rho_{w0}\tau_{f0}$ controls the transition between pyrolysis and char oxidation processes.

Considering the char oxidation process, we can conclude from a dimensional analysis similar to that derived in [7] that the characteristic time for total char oxidation scales with $\chi_0 = \rho_{w0}D_{f0}^{5/3}\tau_{f0}^{-1/6}$. As a flying firebrand loses volume only from char oxidation, it can be expected that whether the brand burns totally in the air or lands on the ground is affected by the burning parameter χ_0 . It will be shown below that the char content, v_c , which is related to the kind of wood, also plays an important role in the characteristics of the transport of firebrands. For wildland fuels, it is less than 0.4.

3.3. Landing criterion

There exists a critical value of χ_0 above which a firebrand will necessarily land before being entirely consumed. This value is determined graphically by plotting the distances covered by 10,000 firebrands as a function of the burning parameter. An example is given in Fig. 2 of firebrands generated from the burning bark of Ponderosa pine ($v_c = 0.39$ [15]) lofted by a 30 MW m^{-1} line fire and transported by a wind velocity of 11.17 m s^{-1} .

Numerical experiments show that the critical value, $(\chi_0)_{cr}$, depends on fire intensity, wind conditions, and fuel type through the char content, v_c . Fig. 3a shows that, for a 30 MW m^{-1} line fire and a wind velocity of 11.17 m s^{-1} , the critical value decreases exponentially as a function of v_c . For firebrands of Ponderosa pine, the dependence of $(\chi_0)_{cr}$

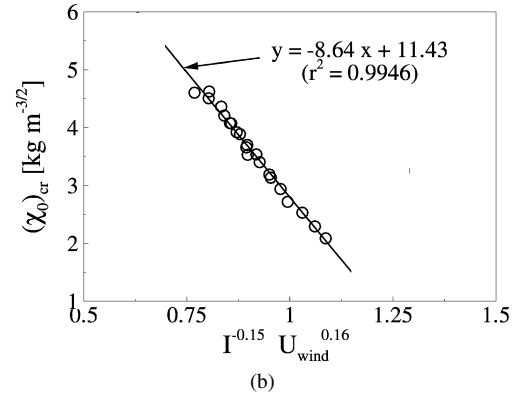
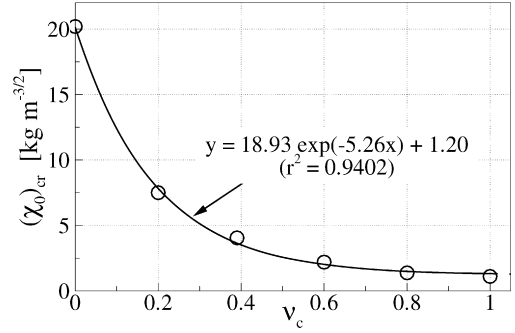


Fig. 3. (a) Critical value of the burning parameter as a function of v_c for a fire intensity of 30 MW m^{-1} and a wind speed of 11.17 m s^{-1} . Although unrealistic for wildland fuels, values of v_c greater than 0.4 are considered in order to highlight the functional dependence of $(\chi_0)_{cr}$ on v_c . (b) Critical value of the burning parameter as a function of $I^{-0.15}U_{wind}^{0.16}$ for $v_c = 0.39$.

on fire intensity and wind speed is illustrated in Fig. 3b.

3.4. Remaining mass at landing

Fig. 4 shows that the normalized mass of the firebrands that land while pyrolysis is still occurring (flaming state) is an exponential function of the flight time normalized by the characteristic time of pyrolysis,

$$\frac{M_{final}}{M_0} = 0.97 \exp\left(-\frac{0.0045}{\rho_{w0}\tau_{f0}}t_{flight}\right). \quad (35)$$

For firebrands that undergo only heterogeneous oxidation (char oxidation state) at landing, the remaining normalized mass is a linear function of the flight time normalized by the characteristic time of char oxidation,

$$\frac{M_{final}}{M_0} = -\frac{2.21 \times 10^{-3}}{\chi_0}t_{flight} + 0.36. \quad (36)$$

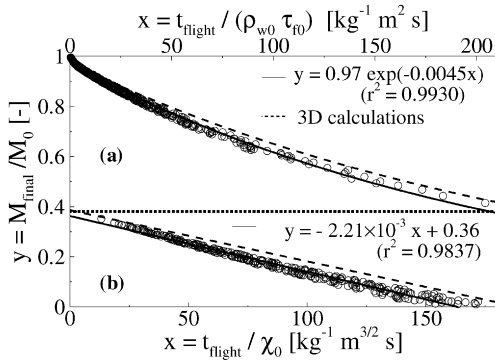


Fig. 4. Remaining mass fraction versus the flight time normalized by $\rho_{w0}\tau_{f0}$ for flaming firebrands at landing (a) or by $\chi_0 = \rho_{w0}D_{f0}^{5/3}\tau_{f0}^{-1/6}$ for firebrands in charring state at landing (b). Here $\nu_c = 0.39$.

These relationships for firebrands transported by plumes above line fires are in good agreement with those obtained by Sardoy et al. [7] in a previous

study concerning the transport of firebrands in a three-dimensional fire-induced plume generated by a group of burning trees (Fig. 4).

3.5. Scattered ground-level distribution of firebrands

The results of the analysis show that, depending on the value of the char content, the ground-level distribution of firebrands exhibits a single or bimodal behavior, whatever the fire intensity and wind speed. Fig. 5 shows the ground-level distribution of firebrands released from a 30 MW m^{-1} fire subjected to a wind of 11.17 m s^{-1} for $\nu_c = 0$, $\nu_c = 0.39$, and “only char oxidation.” $\nu_c = 0$ means that virgin dry wood is totally converted into pyrolysis gases, whereas “only char oxidation” refers to particles that leave the canopy in a charring state. Model results show the existence of a bimodal ground-level distribution of the released firebrands when both pyrolysis and char oxidation are present in the firebrand.

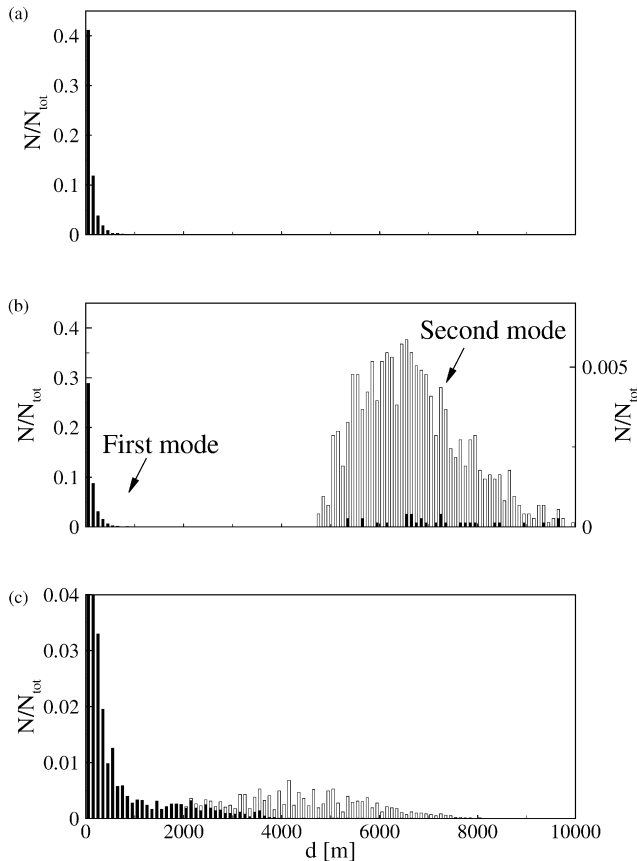


Fig. 5. Ground-level distribution of N_0 fallen firebrands for a fire intensity of 30 MW m^{-1} and a wind speed of 11.17 m s^{-1} for (a) $\nu_c = 0$ and $N_{\text{tot}} = 5052$, (b) $\nu_c = 0.39$ and $N_{\text{tot}} = 7338$, the left-hand scale corresponding to “short-distance” firebrands, the right-hand scale to “long-distance” firebrands, and (c) only “char oxidation process” and $N_{\text{tot}} = 8337$. Black-filled bars correspond to firebrands that land at a temperature higher than 500 K .

For $\nu_c = 0.39$ (Fig. 5b), of the 10,000 brands launched, 7338 reached the ground; the others either burned while in flight or fell inside the canopy. A bimodal distribution was obtained. The first mode was composed of firebrands, referred to as “short-distance” firebrands, that landed on the ground at distances of up to around 1000 m. It included 72.38% of the 7338 firebrands that reached the ground and more than 99% of them landed while still flaming. Such firebrands, which impact the ground in a flaming state, have a high potential to ignite spot fires [16]. The second mode corresponds to “long-distance” firebrands, with a landing distance greater than 4500 m. It exhibits a Poisson-like behavior with a maximum at about 6100 m. Of the fallen firebrands, 27.62% belonged to this mode, and results show that they reached the ground in a char oxidation state. The maximum temperature at landing for the present case was about 550 K, and only 3.26% of the firebrand in the char oxidation state had a temperature greater than 500 K. Their lower temperature combined with smaller remaining mass resulted in a smaller spotting potential.

For $\nu_c = 0$ (Fig. 5a), a single-mode distribution of “short-distance” flaming firebrands was obtained with a potential maximum spotting distance (1128 m) a little longer than the distance reached for the case $\nu_c = 0.39$. The density of the brands continued to tend toward a value of zero, and the parameter $\rho_f \tau_{f0}$ was more significantly affected during the transport, which enhanced the aerodynamic forces on the particle.

When the firebrands were submitted only to char oxidation (Fig. 5c), a single-mode distribution of charring firebrands with a wide range of landing distances was obtained. These firebrands, whose density remained constant during their transport, generally fell nearer the canopy. However, they could have the potential to ignite spot fires at long distances, since 76.12% of them reached the ground with a temperature higher than 500 K and as far away as 4500 m.

3.6. Parameters of the bimodal distribution

As discussed in Section 3.2, the product $\rho_{w0} \tau_{f0}$ determines which firebrands will land in the short- or long-distance regions (Fig. 5b). This is understandable, since this parameter relates aerodynamic and gravitational forces, and consequently the landing distance, as well as controlling the transition between pyrolysis and char oxidation processes.

Fig. 6 shows the landing distance as a function of the parameter $\rho_{w0} \tau_{f0}$ for the 7338 brands of interest, from the 30 MW m⁻¹ fire subjected to a wind of 11.17 ms⁻¹, and for a char content of 0.39. This plot shows three different regions: re-

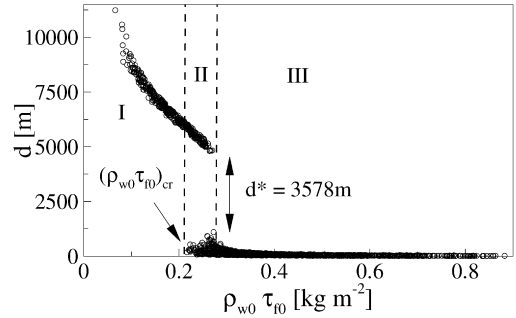


Fig. 6. Landing distance as a function of the parameter $\rho_{w0} \tau_{f0}$ for $\nu_c = 0.39$, a fire intensity of 30 MW m⁻¹, and a wind speed of 11.17 ms⁻¹.

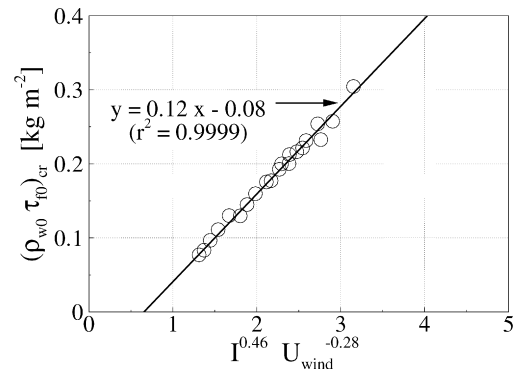


Fig. 7. Critical value of the distribution parameter $(\rho_{w0} \tau_{f0})_{cr}$ as a function of $I^{0.46} U_{wind}^{-0.28}$. Here $\nu_c = 0.39$.

gion I is relative to long-distance firebrands, for which $\rho_{w0} \tau_{f0} < 0.2125$ kg m⁻², whereas region III concerns short-distance firebrands, for which $\rho_{w0} \tau_{f0} > 0.2695$ kg m⁻². When 0.2125 kg m⁻² $\leq \rho_{w0} \tau_{f0} \leq 0.2695$ kg m⁻² (region II in Fig. 6), the corresponding firebrands can travel over a few hundred meters or more than 4500 m depending on their initial location, firebrands initially located close to the centerline traveling the furthest. The value 0.2125 kg m⁻² can be considered for the present case as a critical value, referred to as $(\rho_{w0} \tau_{f0})_{cr}$, beyond which the firebrand may land flaming, with the potential to ignite receptive fuel beds, within a short distance of the fire source. This critical value is a linear function of powers of fire intensity and wind speed, as observed by fitting model results (Fig. 7).

Another important characteristic of the bimodal distribution is the separation d^* between the “short-distance” and the “long-distance” landing firebrands (Fig. 6).

The separation distance d^* between the two modes of distribution depends linearly on the value of ν_c , as is shown in Fig. 8. It is also interesting to note that the value of $(\rho_{w0} \tau_{f0})_{cr}$ is basically inde-

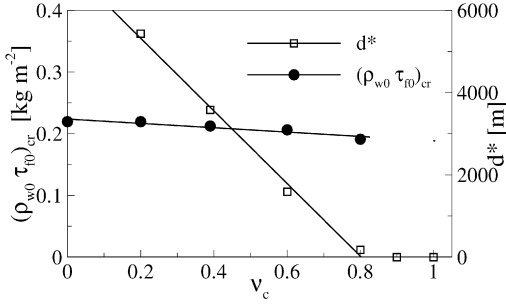


Fig. 8. Critical value $(\rho_{w0}\tau_{f0})_{cr}$ and distance d^* as a function of v_c for a fire intensity of 30 MW m^{-1} and a wind speed of 11.17 m s^{-1} . Although unrealistic for wildland fuels, values of v_c greater than 0.4 are considered in order to highlight the functional dependence of $(\rho_{w0}\tau_{f0})_{cr}$ and d^* on v_c .

pendent of the char content (Fig. 8). These results are potentially important, since v_c depends on the type of wood, and consequently the characteristics of fire spotting depend not only on fire and environment characteristics but also on vegetation type.

3.7. “Short-distance” firebrand distribution

Let us consider now the first mode of the bimodal distribution, which corresponds to “short-distance” firebrands. The x -axis is discretized into intervals of equal size Δd . The interval size is chosen large enough to avoid empty segments and small enough to obtain sufficient detail. The number of particles in each interval is divided by the total number of “short-distance” firebrands, N_{sd} . The “short-distance” firebrand distribution can therefore be approximated by a lognormal function of the landing distance d ,

$$p(d) = \frac{1}{\sqrt{2\pi}\sigma d} \exp\left\{-\frac{(\ln d - \mu)^2}{2\sigma^2}\right\}, \quad (37)$$

where μ and σ are the mean and standard deviation of the logarithm of the variable

$$\mu = \sum_{k=1}^{n_{int}} \frac{N_k}{N_{sd}} \ln d_k, \quad (38)$$

$$\sigma = \sqrt{\sum_{k=1}^{n_{int}} \frac{N_k}{N_{sd}} (\ln d_k - \mu)^2},$$

where n_{int} is the number of intervals involved in the “short-distance” firebrand distribution. Both the distribution and the lognormal function are plotted in Fig. 9 for $v_c = 0.39$, a fire intensity of 30 MW m^{-1} and a wind speed of 11.17 m s^{-1} .

This lognormal behavior confirms the experimental observations made during the 2001 Spotfire

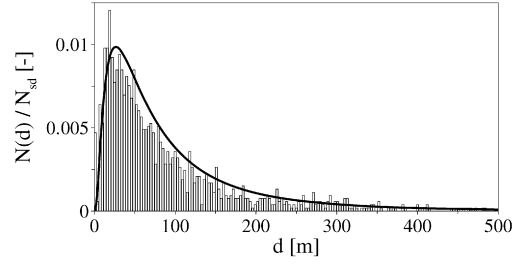


Fig. 9. Ground-level distribution of “short-distance” firebrands for $v_c = 0.39$, a fire intensity of 30 MW m^{-1} , and a wind speed of 11.17 m s^{-1} . The fitting curve corresponds to the lognormal function $p(d) = \frac{1}{\sqrt{2\pi}\sigma d} \exp\left\{-\frac{(\ln d - \mu)^2}{2\sigma^2}\right\}$ with $\mu = 4.20$ and $\sigma = 0.96$.

project [17], which reported that the ground-level distribution reaches a maximum near the fire front and that this maximum is followed by an exponential decrease. It is also in qualitative agreement with the numerical results obtained by Himoto and Tanaka [6].

To illustrate how fire and wind conditions affect the first mode of the bimodal distribution, it is necessary to introduce the Froude number, $Fr = U_{wind}/\sqrt{gL_c}$, based on the characteristic length of the plume,

$$L_c = \left(\frac{10^3 \times I}{\rho_{\infty} c_{pg} T_{\infty} g^{1/2}}\right)^{2/3}.$$

For the plumes considered, two regimes are identified: a buoyancy-driven regime ($Fr < 1$) and a wind-driven regime ($Fr > 1$). A least-squares fitting of model results is performed for both regimes. It is found that the two parameters of the lognormal function, μ and σ , follow an affine relationship with powers of the fire intensity and wind speed (Fig. 10).

4. Conclusions

A numerical study was performed to determine the ground-level distribution of disk-shaped firebrands released into a plume rising above a line fire, as well as their state on landing. When both in-depth pyrolysis (flaming) and char oxidation occur during the transport of the firebrand, a bimodal distribution of landing sites is found. “Short-distance” firebrands land while still pyrolyzing (flaming), whereas “long-distance” ones reach the ground in a char oxidation state. The spacing between the two landing sites depends on the char content. Whether a firebrand will land in one or another landing site depends on the parameter $\rho_{w0}\tau_{f0}$. The remaining normalized mass of firebrands in the flaming state at landing is found to be an exponential decay of the flight time normalized by the product $\rho_{w0}\tau_{f0}$, and for firebrands that reach the ground in

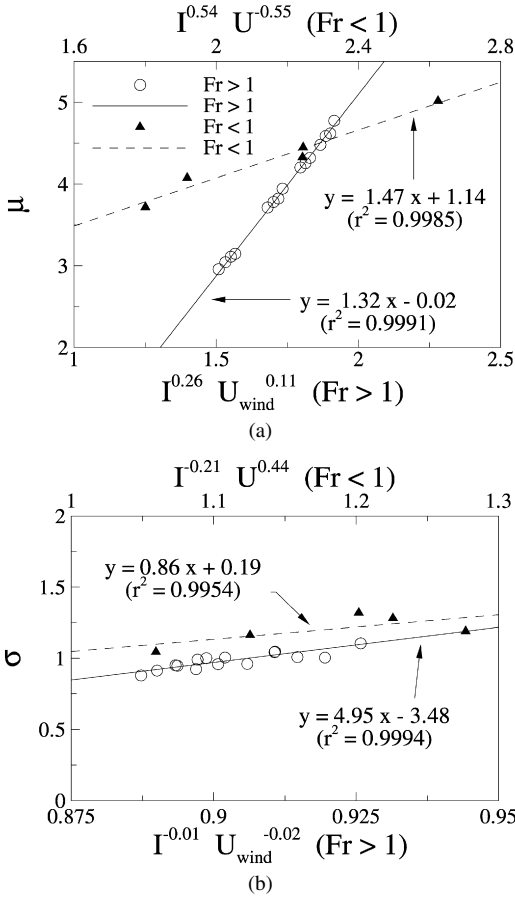


Fig. 10. Parameters of the lognormal function: (a) μ vs. $I^{0.54} U^{-0.55}$ for $Fr < 1$ and μ vs. $I^{0.26} U_{wind}^{0.11}$ for $Fr > 1$, (b) σ vs. $I^{-0.21} U^{0.44}$ for $Fr < 1$ and σ vs. $I^{-0.01} U_{wind}^{-0.02}$ for $Fr > 1$. Here $\nu_c = 0.39$.

the charring state, there is a linear relationship between their remaining normalized mass at landing and the flight time normalized by $\chi_0 = \rho_{w0} D_{f0}^{5/3} \tau_{f0}^{-1/6}$. There exists a critical value of χ_0 above which a firebrand will necessarily land before being entirely consumed. This critical value appears to be dependent on ν_c and on the wind speed and fire intensity. For those of the “short-distance” firebrands that have the potential to ignite new secondary fires because they are flaming and have significant mass at landing, the ground-level distribution follows a lognormal function. The function parameters, i.e., the mean travel distance and its standard deviation, can be determined from correlations in terms of fire intensity and wind speed. The results of this work, in particular the lognormal function that describes the distribution of short-distance landing firebrands and the relevant

problem parameters that describe the separation between the short- and long-distance landing regions and determine whether the firebrands will burn in the air or land on the ground, could be incorporated easily into fire propagation models in order to predict the potential spotting characteristics of a wildland fire.

References

- [1] C.S. Tarifa, P.P. Del Notario, F.G. Moreno, Proc. Combust. Inst. 10 (1965) 1021–1037.
- [2] S.L. Lee, J.M. Hellman, Combust. Flame 15 (1970) 265–274.
- [3] F.A. Albini, Combust. Sci. Technol. 32 (1983) 277–288.
- [4] J.P. Woycheese, P.J. Pagni, Combustion models for wooden brands, in: Proc. 3rd Int. Conf. on Fire Research and Engineering, Society of Fire Protection Engineers, Washington, USA, 1999, p. 53.
- [5] R.A. Anthenien, S.D. Tse, A.C. Fernandez-Pello, Fire Safe. J. 41 (2006) 349–363.
- [6] K. Himoto, T. Tanaka, Transport of disk-shaped firebrands in a turbulent boundary layer, in: Proc. 8th Int. Symp. on Fire Safety Science, Beijing, China, 2005, p. 433.
- [7] N. Sardoy, J.L. Consalvi, B. Porterie, A.C. Fernandez-Pello, Combust. Flame 150 (2007) 151–169.
- [8] E. Koo, P. Pagni, R. Linn, Using FIRETEC to describe firebrand behavior in wildfires, in: Proc. 10th Int. Conf. and Exhibition on Fire and Materials, San Francisco, CA, 2007.
- [9] G.N. Mercer, R.O. Weber, Int. J. Wildland Fire 4 (1994) 201–207.
- [10] D.V. Schroeder, Thermal Physics, Addison–Wesley–Longman, 1999.
- [11] G.A. Davidson, Atmos. Environ. 20 (1986) 471–478.
- [12] C. Yin, L. Rosendahl, S.R. Kaer, H. Sorensen, Chem. Eng. Sci. 58 (2003) 3489–3498.
- [13] C. Lindenburg, Stall coefficients, aerodynamic airfoil coefficients at the large angle of attack, in: Proc. IEA Symp. on the Aerodynamics of Wind Turbines, ECN-RX-01-004, NREL, USA, 2000.
- [14] S.D. Tse, A.C. Fernandez-Pello, Fire Safe. J. 30 (1998) 333–356.
- [15] A.M. Grishin, Mathematical Modeling of Forest Fires and New Methods of Fighting Them, Pub. House of the Tomsk University, Tomsk, 1997.
- [16] S.L. Manzello, T.G. Cleary, J.R. Shields, J.C. Yang, Urban-wildland fires: On the ignition of surfaces by embers, in: Proc. 4th Joint Meeting of the U.S. Sections of the Combustion Institute, The Combustion Institute, Philadelphia, USA, 2005, p. 1.
- [17] P.F. Ellis, Spotting and firebrand behaviour in dry eucalypt forest and the implications for fuel management in relation to fire suppression and to ember (firebrand) attack on houses, in: Proc. 3rd Int. Wildland Fire Conference, Sydney, 2003.